Supplemental Materials for

Optically-controlled dielectric metasurfaces for dynamical dual-mode modulation on terahertz waves

Haoyang Zhou [1,†], Sheng Zhang[1,†], Shunjia Wang[1,†], Yao Yao[1],Qingnan Cai[1], Jing Lin[1], Xiaoying Zheng[1], Zhuo Wang[1], Zhensheng Tao[1,*], Qiong He[1,*]and Lei Zhou[1,*]

[1] State Key Laboratory of Surface Physics, Key Laboratory of Micro and Nano Photonic Structures (Ministry of Education) and Physics Department,

Fudan University, Shanghai 200433, People's Republic of China

*Corresponding Authors: Zhensheng Tao, Email: zhenshengtao@fudan.edu.cn

Qiong He, Email: qionghe@fudan.edu.cn

Lei Zhou, E-mail: phzhou@fudan.edu.cn

†These authors contributed equally to this work
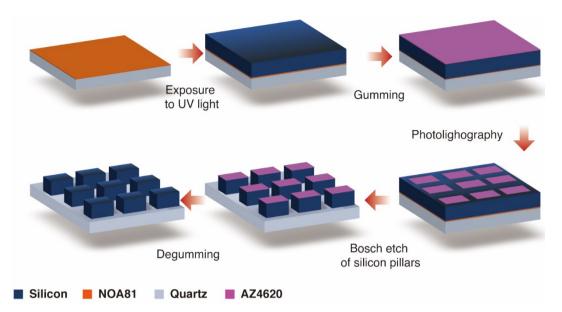
I. Details of sample fabrication

Exposure to UV light

Gumming

Photolighography

Degumming

Bosch etch of silicon pillars

- Silicon
- NOA81
- Quartz
- AZ4620

Fig. S1 Schematic of sample fabrication process.

Quartz substrate is firstly bonded to the high-resistivity silicon (>10000 $\Omega \cdot cm$) wafer with a thin layer of spin-coated UV curable polymer optical adhesive (Norland Optical Adhesive 81) and then exposed to UV light for about 10 min. Then we use standard UV photolithography to make the designed patterns on the silicon side of hybrid silicon-quartz wafer. The silicon wafer is then etched by a deep reactive ion etching (DRIE) procedure and each cycle of Bosch process contains passivation for 3 s and etching steps for 8 s. These process cycles are repeated for about 160 times and silicon is then completely removed with pillars attached on quartz substrate. Residual photoresist on top of silicon pillars is finally removed using plasma cleaning.
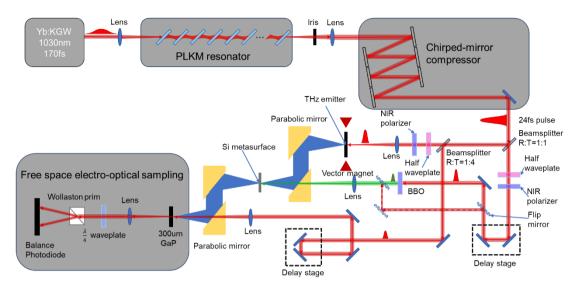
II. Experimental details

Fig. S2 Schematic of the Experimental setup.

Fig. S2 depicts the schematic of the home-make optical pump terahertz probe experiment setup. Ultrafast laser pulses are generated by an efficient pulse compression system of a Yb: KGW laser amplifier (with a pulse duration of 170 fs at $\lambda = 1030$ nm) with periodic layered Kerr media (PLKM)[60]. Laser pulses with 80 µJ energy and 100kHz repetition rate are focused to a beam with a diameter of 140 µm. Ultra-short pulses with a duration of ~24 fs and an energy of 60 µJ were generated after pulse compression.

As shown in Fig. S2, a compressed femtosecond pulse is delivered to excite the spintronic terahertz emitters which are composed of ferromagnetic and nonferromagnetic film. The polarization orientation of terahertz emission from spintronics terahertz emitters is perpendicular to the direction of magnetization. A small portion (~10%) of energy is used as a probe pulse of the free space electro-optical sampling (EOS). The standard EOS detection system, which is composed of a 300-µm GaP crystal, a quarter-waveplate, a Wollaston prism and two balanced photodiodes, is used to measure the time domain signal of the terahertz electric field.

Half of the energy of the ultra-short pulse excites the metasurface sample of silicon which is placed between the second and third parabolic mirror. Also, energy of the optical pump pulse is attenuated by a combination of NIR half waveplate and polarizer.

The terahertz wave is focused to a beam with a diameter of 1.6 mm on the surface of the silicon metasurface sample. The optical pump light is normally incident on the sample with a beam diameter bigger than 1.6 mm to ensure proper excitations of carriers in silicon. Wavelength of the optical pump light can be easily changed between 515nm and 1030nm by switching the optical path between BBO crystal and no BBO crystal.
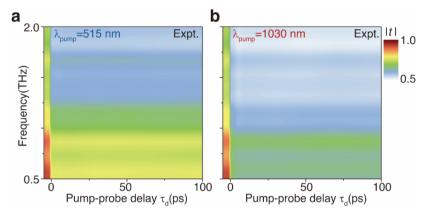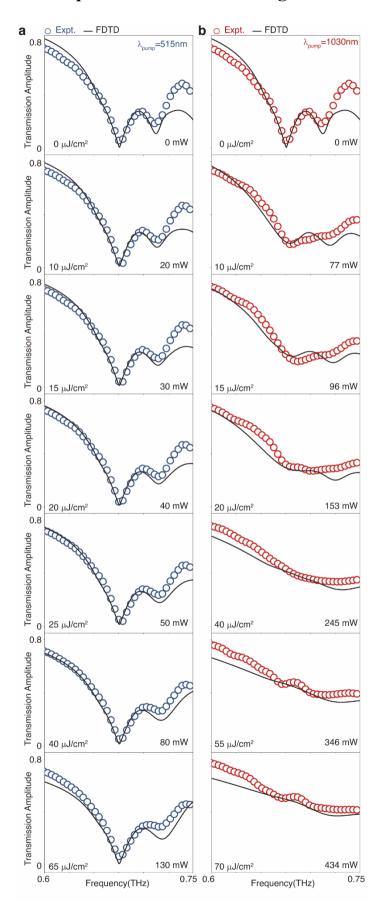

Fig. S3 Measured transmission spectra of optically pump silicon film. a, b Transmission amplitude spectra modulation obtained from fast Fourier transform with the variation of pump-probe delay τ_d.

As a benchmark text, we measured the bared silicon film under the different pump wavelength as depicted in the main text. Fig. S3. Both of Fig. S3a and S3b show a full-band (0.5-2 THz) transient modulation. The pump-probe delay τ_d is selected to be 50 ps as the modulation of silicon is saturated.

III. Additional experimental results for Fig. 2 in the main text

Fig. S4. **Measured (open circles) and FDTD-simulated (solid lines) transmission amplitude spectrum of our meta-device under the photoexcitation of 515nm (a) and 1030nm (b) pump light with different optical fluences, respectively.** The optical fluence F used in the FDTD simulation and measured power of pump pulse in the experiment are labeled at the bottom left and right corner, respectively.

Figs. S4a and S4b depict the additional experimental and simulated transmission spectra of our meta-devices under with different optical fluence F. In our work, the optical fluence F that we considered in our simulation is the fluence that has been effectively used to excite the excess carriers in silicon. Actually, about half of 1030-nm pump light is transmitted through the silicon and thus cannot be absorbed by the silicon to excite carriers. As a result, the optical fluence F that we consider is equal to

$$(1-T_{Si})F_{\text{expt}}=(1-T_{Si})\frac{\text{pump energy}}{S_{\text{pump}}}$$. For the 515 nm - pump case, the pump beam diameter is equal to 1.6 mm and $T_{Si}=0$. For the 1030 nm - pump case, the beam diameter of pump light is equal to 2 mm and $T_{Si}=0.5$. The corresponding relationships between optical fluence F considered in our simulations and the measured fluence F_{expt} are depicted in Figs. S5a-b.
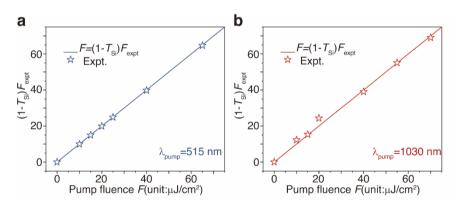

Fig. S5. **Relations between optical fluence** F **considered in our simulations and the experimentally measured fluence** F_{expt}**.**
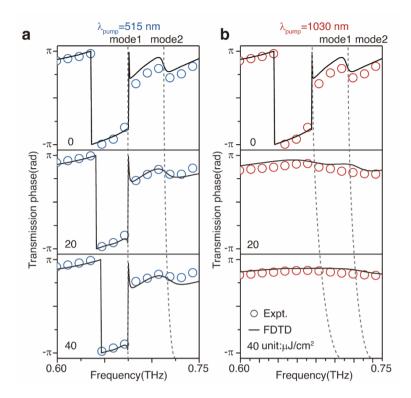
Fig. S6. Measured (symbols) and FDTD-simulated (lines) transmission phase spectra of our meta-device under the photoexcitation of 515nm (a) and 1030nm (b) pump light with optical fluence varying from 0 to $40~\mu J/cm^{2}$, respectively.

The change of transmission phase spectra obtained by OPTP system and FDTD simulation results also reveal a dynamic dual-mode modulation. Two clear phase jumps, representing the two resonant modes possessed by our metasurface, are observed in the top panel. Meanwhile, the phase variation of *mode 2* decreases with the increase of pump fluence, indicating a modulation of *mode 2*. By contrast, the phase jump of *mode 1* holds steady, showing a mode-*selective* modulation. However, when the pump wavelength is switched to 1030 nm, the transmission phase variation of two resonant modes both vanishes, and resulting in a mode-*unselective* modulation.

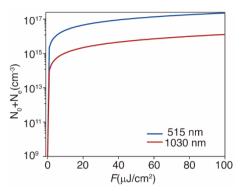# IV. Simulation details of optically tunable silicon metasurface

Fig. S7 Photoexcited carrier density of silicon as function of optical pump fluence for 515nm- (blue) and 1030nm-(red) pump lights.

Number of photoexcited excess carriers is a crucial parameter in our simulation, which depends on the optical fluence F and it can be estimated using the following equation:

$$N_e(F) = [(1 - R_{Si})F(\frac{\alpha}{E_{ph}} + \frac{\beta(1 - R_{Si})F}{2E_{ph}\tau})] \tag{S1}$$

where $\tau = 24$ fs is the pulse width, R_{Si} is the reflectivity of pump pulse by silicon metasurface, $\beta = 6.8$ cm GW^{-1} is the two-photon absorption coefficient parameter. α and E_{ph} are the linear absorption coefficient parameter and the photon energy, respectively, both of which are pump wavelength dependent. The evolution of sum of N_0 and N_e as function of pump fluence at different pump wavelength is shown in Fig. S7, with $N_0 = 5 \times 10^9$ cm^{-3} being the excess carrier of the intrinsic silicon.

As a benchmark test, we measured the transmission amplitude of a 170 μm -thick bared silicon substrate with and without photoexcitation, respectively. The optical fluence is $15 \, \mu J/cm^2$ and $\lambda_{pump} = 1030$ nm . As shown in Fig. S8, measured, numerical simulated and analytically calculated data are in good agreement, proving that model introduced using Equation. (S1) can describe the changes in silicon properties well.

In our FDTD simulations, periodic boundary condition are imposed at the boundaries for x/y-directions and open boundary conditions are imposed for the z direction, respectively. Permittivity of quartz substrate is set as 3.4 with a conductivity of 5 S/m. Measured and calculated transmission spectra of two bare quartz substrates with thickness $90 \mu m$ and $120 \mu m$ are shown in Fig. S9, respectively. $\tilde{\varepsilon}$ of silicon used in our simulation is determined by the Drude model with appropriate carrier densities in the doped and undoped regions. NOA81 layer is ignored because it is too thin to influence the final optical response. In the application II section, we treat Gold as lossy metal of conductivity 1×10^{6} S/m in THz regime.
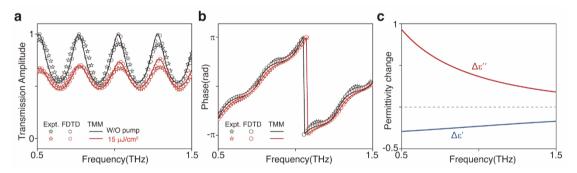

Fig. S8 Experimental study of the dynamic tuning ability of 170 μm-thick silicon film. a Measured (stars), simulated (circles) and calculated (lines) transmission amplitude spectra of bared silicon film. The transmissions decrease as the pump fluence is tuned from 0 to 15 μJ/cm². **b** Measured (stars), simulated (circles) and calculated (lines) transmission phase spectra of bared silicon film. **c** Real ($\Delta\varepsilon'$) and imaginary ($\Delta\varepsilon''$) parts of permittivity change of silicon used in simulation and Transfer Matrix Method (TMM) calculation, obtained from Drude model equation illustrated in the main text.
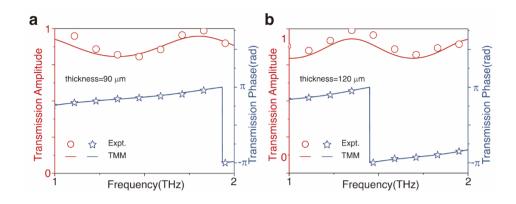
Fig. S9 Measured and calculated transmission amplitude and phase of bared quartz substrate with thickness is equal to 90 μm **(a) and** 120 μm **(b).**

V. Details of Quasi-normal-mode perturbation theory
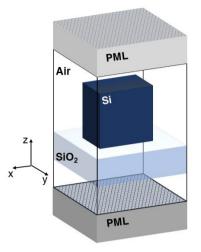
i. QNM simulation setup

Fig. S10 Schematic of the QNM simulation setup for the uniform metasurface.

Resonant modes (called also as quasi-normal modes) inside a resonator exhibit distinct electromagnetic field distributions $\{\tilde{\mathbf{E}}_n^{(0)} \ \tilde{\mathbf{H}}_n^{(0)}\}$ that satisfy Maxwell equations in the absences of sources:

$$\nabla \times \tilde{\mathbf{E}}_n^{(0)} = -i\tilde{\omega}_n^{(0)} \boldsymbol{\mu}(\tilde{\omega}_n^{(0)}) \tilde{\mathbf{H}}_n^{(0)}$$
$$\nabla \times \tilde{\mathbf{H}}_n^{(0)} = i\tilde{\omega}_n^{(0)} \boldsymbol{\varepsilon}(\tilde{\omega}_n^{(0)}) \tilde{\mathbf{E}}_n^{(0)}$$

$$(S2)$$

with subscripts n denoting the nth unperturbed resonant mode and $\tilde{\omega}_n^{(0)}$ representing its unperturbed complex eigen frequency. Such an EM wave field distribution could be numerically calculated using a FEM method, which is schematically shown in Fig. S10. Here, perfect matched layers (PML) are adopted at the top and bottom sides of the simulation domain to absorb all light energy radiate outside, and thus cut off the diverging EM field along $\pm z$ directions.

ii. Normalization factor used in QNMPT

Perturbation theory is then adopted to calculate the change of eigen-frequencies of QNM modes under different external pumping conditions. Utilizing the EM wave distributions of different eigenmodes calculated with the QNM method, we can use the

following equation $\Delta\tilde{\omega}_{\mathrm{n}} = \dfrac{-\tilde{\omega}_n^{(0)} \cdot \iiint \Delta\tilde{\varepsilon}(\vec{r})\tilde{\mathbf{E}}_{\mathrm{n}}^{(p)}(\vec{r})\cdot\tilde{\mathbf{E}}_{\mathrm{n}}^{(0)}(\vec{r})d\vec{r}}{\iiint\limits_{\Omega} \{\tilde{\mathbf{E}}_{\mathrm{n}}^{(0)} \cdot \frac{\partial[\omega\varepsilon]}{\partial\omega}\tilde{\mathbf{E}}_{\mathrm{n}}^{(0)} - \tilde{\mathbf{H}}_{\mathrm{n}}^{(0)} \cdot \frac{\partial[\omega\mu]}{\partial\omega}\tilde{\mathbf{H}}_{\mathrm{n}}^{(0)}\}d^3\vec{r}}$ to analytically

calculate the frequency shift of the n-th eigenmode. We note that the denominator

$\iiint\limits_{\Omega} \{\tilde{\mathbf{E}}_{\mathrm{n}}^{(0)} \cdot \frac{\partial[\omega\varepsilon]}{\partial\omega}\tilde{\mathbf{E}}_{\mathrm{n}}^{(0)} - \tilde{\mathbf{H}}_{\mathrm{n}}^{(0)} \cdot \frac{\partial[\omega\mu]}{\partial\omega}\tilde{\mathbf{H}}_{\mathrm{n}}^{(0)}\}d^3\vec{r}$ is the normalization factor, and we can use

it to get the normalized quasi eigen-wavefunctions which are presented in Eq. (2) of the

main text. The integral volume Ω is the whole space including the PML layers as

shown in Fig. S10. In addition, as mentioned in the article, the perturbed electric field

denoted by $\tilde{\mathbf{E}}_{\mathrm{n}}^{(p)}(\vec{r})$ can be derived from the unperturbed one $\tilde{\mathbf{E}}_{\mathrm{n}}^{(0)}(\vec{r})$ using local field

correction[56]: $\tilde{\mathbf{E}}_{\mathrm{n}}^{\perp(p)}(\vec{r}) \approx \dfrac{\varepsilon^{(0)}}{\tilde{\varepsilon}^{(p)}}\tilde{\mathbf{E}}_{\mathrm{n}}^{\perp(0)}(\vec{r}), \tilde{\mathbf{E}}_{\mathrm{n}}^{\|(p)}(\vec{r}) \approx \tilde{\mathbf{E}}_{\mathrm{n}}^{\|(0)}(\vec{r})$, where superscript $\perp$ ($\|$) refers

to normal (tangential) field components.

iii. Reasons for the distinct evolution behavior of real and imaginary parts of $\Delta\tilde{\omega}_{\mathrm{n}}$ for two resonant modes in the case of 1030 nm

In the main text, we find that in the case of $\lambda_{\mathrm{pump}} = 1030\ \mathrm{nm}$, the two

$\mathrm{Re}(\Delta\tilde{\omega}_{\mathrm{n}}) \sim F$ relations exhibit different variation slopes as compared to their

corresponding $-\mathrm{Im}(\Delta\tilde{\omega}_{\mathrm{n}}) \sim F$ counterparts in the case of $\lambda_{\mathrm{pump}} = 1030\ \mathrm{nm}$. Such an

intriguing phenomenon is essentially caused by different phases carried by the complex

integrals $\tilde{A}_n = \iiint\limits_{\vec{r}\in\mathrm{P.R.}} \tilde{\mathbf{E}}_{\mathrm{n}}^{(p)}(\vec{r})\cdot\tilde{\mathbf{E}}_{\mathrm{n}}^{(0)}(\vec{r})d\vec{r}$ presented in Eq. (2) of the main text, for

different resonant modes. We emphasize that the integrations in above equation are only

performed within the perturbed region, not the whole space Ω as we calculate the

normalization factor. In principle, the integral $\iiint\limits_{\vec{r}\in\mathrm{P.R.}} \tilde{\mathbf{E}}_{\mathrm{n}}^{(p)}(\vec{r})\cdot\tilde{\mathbf{E}}_{\mathrm{n}}^{(0)}(\vec{r})d\vec{r}$ is not a real

value but is a complex number with amplitude and phase sensitively depending on the

mode index n and the perturbed region. We note that here $\{\tilde{\mathbf{E}}_{\mathrm{n}}^{(p)}(\vec{r}), \tilde{\mathbf{E}}_{\mathrm{n}}^{(0)}(\vec{r})\}$ are already

normalized wave-functions, and thus they have unambiguously determined phases at

every local point. To illustrate the physic only, we replace $\tilde{\mathbf{E}}_n^{(p)}(\vec{r})$) by $\tilde{\mathbf{E}}_n^{(0)}(\vec{r})$ to calculate $\tilde{A}_n$ under two different pump wavelengths, and list the obtained results in Table S1. Clearly, we find that in the case of 1030 nm, $\tilde{A}_n$ of two modes are of comparable amplitudes and different phases. We note that the term $\tilde{\omega}_n^{(0)} \cdot \Delta\tilde{\varepsilon}$ in Eq. (2) discussed in the main text, which is linearly proportional to F, is also a complex number. Therefore, the product of two complex numbers $(\tilde{\omega}_n^{(0)} \cdot \Delta\tilde{\varepsilon}) \cdot \tilde{A}_n$ must lead to distinct fluence F dependences for the real and imaginary parts of $\Delta\tilde{\omega}_n$, sensitively depending on the phases of $\tilde{A}_n$.

We find that the 515 nm case exhibits a different behavior. In this case, $\left|\tilde{A}_1\right|$ is an order of magnitude smaller that $\left|\tilde{A}_2\right|$. Although $\tilde{A}_n$ of two modes also exhibit different phases, such drastic amplitude difference now dominates the behavior of $\Delta\tilde{\omega}_n \sim F$ relationship and thus results in a mode-selective modulation phenomenon discussed in the main text.
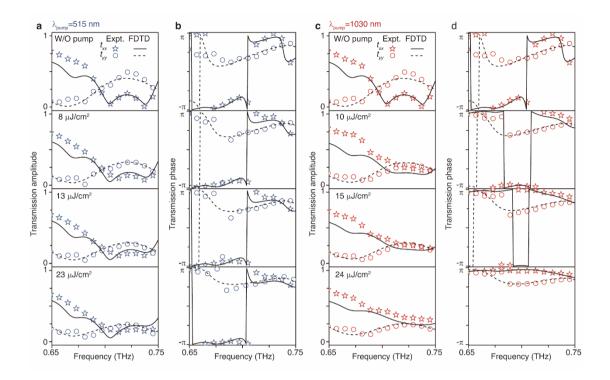
Table S1. Complex field integral calculation results

$\tilde{A}_n \varepsilon_0$	$\lambda_{pump} = 515$ nm	$\lambda_{pump} = 1030$ nm
Mode 1	$(1.79 - 0.54i) \times 10^6\, \varepsilon_0$	$(3.27 + 1.96i) \times 10^9\, \varepsilon_0$
Mode 2	$(1.19 + 0.03i) \times 10^7\, \varepsilon_0$	$(2.23 - 0.30i) \times 10^9\, \varepsilon_0$

VI. Potential materials for dynamic multi-mode modulation at mid infrared (MIR) and near infrared (NIR) frequency regime.

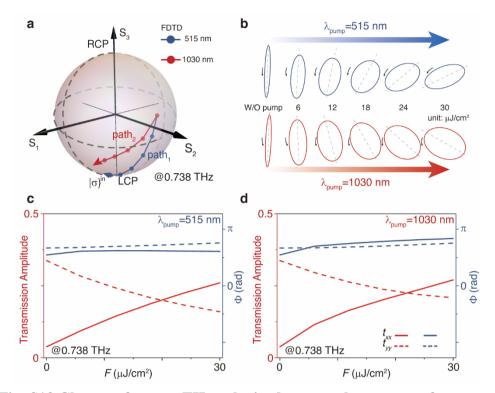**Table S2**. Common semiconductors and related parameters

Semiconductors	GaAs	GaN
Range of λ_{pump} (nm)	$500 \sim 870$	$150 \sim 294$
Range of δ	$88 \text{ nm} \sim 10 \text{ μm}$	$7 \text{ nm} \sim 400 \text{ nm}$
Working frequency regime	MIR	NIR
References	[61]	[62]

VII. Additional experimental results of dynamic multi-mode polarizer

Fig. S11 Additional experimental/simulation data for the sample studied in Fig. 4 of the main text, shined by x and y polarized light with different optical fluence, respectively. Measured (denoted using stars and open circles) and simulated (denoted using solid and dashed lines) results of the transmission amplitude (a, c) and phase spectra (b, d) under the pump of 515nm (a, b) and 1030nm (c, d) with the increase of pump fluence F
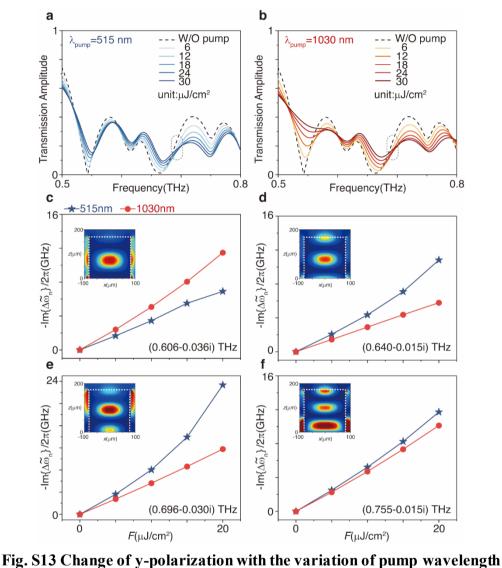
VIII. Change of polarization states at a frequency near *mode 2.*

Fig. S12 Change of output THz polarized state at the resonant frequency near mode 2. a FDTD-simulated pump-wavelength trajectories on the Poincare's sphere for transmitted THz waves at 0.738 THz with different pump fluences showing dynamic range in tunability of the polarization state. **b** simulated polarization states under the photoexcitation of 515-nm (blue) and 1030-nm (red) pump light with different pump fluence. **c, d** simulated evolutions of transmission amplitude and phase as function of pump fluence under photoexcitation of 515 nm (c) and 1030 nm (d) pump light, respectively.

In the main text, we discussed the evolution of polarization states at the frequency at 0.695 THz, which is close to the resonant frequency of *mode 1*. Here, to further prove the dual-mode modulation ability of our proposed meta-polarizer, we show in Fig. S12a the evolution paths of output THz polarization states at 0.738 THz (resonant frequency of *mode 2*). Similar to the case studied in the main text, here we also find two paths on Poincare's sphere corresponding to two pump wavelengths, again demonstrating the expanded polarization-control capability of the meta-device.

IX. Additional discussions on the y-polarization transmission properties of the meta-device studied in Fig. 4

Fig. S13 Change of y-polarization with the variation of pump wavelength and pump fluence. a, b FDTD-simulated transmission spectra of y polarization under the pump of 515 nm (a) and 1030 nm (b) pump pulse with varying pump fluences from 0 to 30 $\mu J/cm^2$. The working frequency band discussed in the main text is denoted using a dashed frame. **c-f** Numerically simulated negative imaginary parts of $\Delta\tilde{\omega}_n$ for the supported resonant modes as function of optical fluence of photoexcitation of 515 nm (blue dotted lines)- and 1030 nm (red dotted lines)-pump light, respectively. Upper left inset shows the corresponding field pattern of each resonant modes. Areas inside the white

dotted lines denote the silicon pillar and the rest area is vacuum. Their numerically simulated eigen-frequencies $\tilde{\omega}_n / 2\pi$ are shown at the bottom right corners, respectively.

In the main text, we find that the evolution of t_{yy} shows similar F-dependent behaviors for two pump-light wavelengths. As can be seen in the Figs. S13a-b, variations of $|t_{yy}|$ at 0.695 THz due to increasing F are indeed rather weak. We find that this is because that transmission at this frequency is influenced by several high-order y-polarized modes at frequencies below 0.695 THz, which exhibit low quality factors. These high-order y-polarized modes, with resonant wave-functions depicted in the insets to Fig. S13(c-f), have strong E fields on the pillar surface. Therefore, all these modes can be affected by both 515 nm and 1030 nm pump pulse, as seen from the evolution of $-\mathrm{Im}(\Delta\tilde{\omega}_n) \sim F$ relation depicted in Figs. S13c-f (515 nm and 1030 nm pump case have similar behavior). Meanwhile, the working frequency 0.695 THz is located between distinct resonant modes frequencies and thus $|t_{yy}|$ shows pump-fluence-insensitive for both pump excitations.
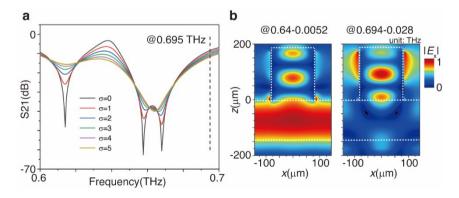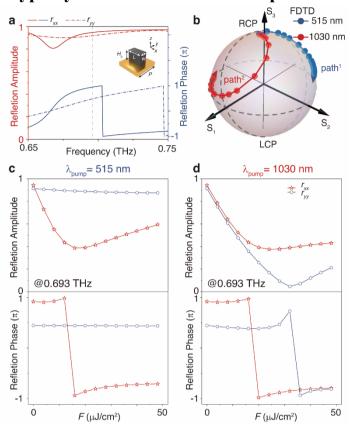

Fig. S14 High-order modes supported by meta-atom around 0.66THz. a FDTD-simulated transmission spectra of y polarization with the variation of the loss of quartz substrate from 0 to 5 S/m. The dashed line denotes the working frequency of our proposed meta-polarizer. **b** Electric field spatial

distribution of eigen modes supported by meta-atom around 0.66 THz calculated at lossless background. Areas inside the white dotted lines denote the silicon pillar and quartz substrate while the rest area is vacuum. Their numerically simulated eigen-frequencies $\tilde{\omega}_{n} / 2\pi$ are shown at the top sides, respectively.
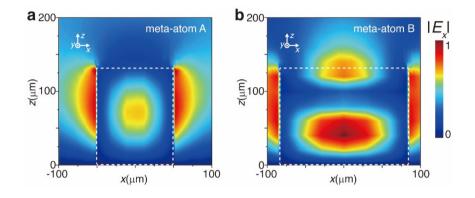
In the main text, a broadband dip is found in the $|t_{yy}|$ spectrum around 0.66 THz in Fig. 4. However, as shown in Fig. S14a, when we reduce the loss factor of the quartz substrate, two dips are clearly observed in the FDTD-simulated transmission spectrum, indicating that two higher-order modes are now coupled together around 0.66 THz. Corresponding numerically simulated QNMs are shown in Fig. S14b.

X. Reflection-type dynamic-dual mode meta-polarizer

Fig S15. Numerical demonstration of a reflection-type dual-mode meta-polarizer with expanded polarization control ability. a FDTD-simulated spectra of reflection amplitude and phase of proposed metasurfaces shown in the inset under the illumination of x polarized and y polarized THz light, respectively. Gray dashed line denotes the working frequency 0.693 THz. **b** FDTD-simulated polarization trajectories on Poincare's sphere of THz waves at 0.693 THz reflected by metadevice pumped by external light at different wavelengths with varying pump fluences. The incident THz wave is -45° linear polarized. **c, d** Simulated evolutions of transmission amplitude and phase as function of pump fluence under photoexcitation of 515 nm (c) and 1030 nm (d) pump light, respectively. Geometrical parameters of meta-atom : $W=76, L=150, H_q=130, P=288$, all in units of μm.

XI. Additional information for the optical information encryption meta-device

i. QNMs supported by meta-atom A&B at working frequency

Fig. S16 Normalized electric field spatial distribution of eigen modes supported by meta-atom A&B discussed in Fig. 5 at 0.63 THz. Areas inside the white dotted line denote the silicon pillar and the rest area is vacuum.

From Fig. S16, we find that the excited electric field of the eigen mode supported by meta-atom A concentrates inside the silicon pillar. However, for meta-atom B, the relevant resonant mode is a higher order mode and thus it is easy to be perturbed by short wave photoexcitation.

ii. Dyadic Green's function approach used in optical information encryption meta-devices

Due to the limitation of numerical computing resources, we utilized the dyadic green's function method to calculate the THz field pattern generated by our proposed optical-information-encryption meta-device, as it is shined by normally incident x-polarized THz wave at 0.63 THz under different photoexcitation.

By illuminating a normally incident x-polarized terahertz wave with frequency ω, our proposed meta-device can generate a surface current distribution $\tilde{\boldsymbol{J}}(\bar{r}',\omega)$ (located at plane $z = 0$), and then the corresponding output field pattern

$\tilde{E}(\vec{r}, \omega)$ (located at plane $z = 25\lambda$) can be calculated using the following equation:

$$\tilde{E}(\vec{r}, \omega) = i\omega\mu_0 \int \ddot{G}(\vec{r}, \vec{r}')\tilde{J}(\vec{r}', \omega)d\vec{r}' \qquad (S3)$$

In our calculations, the surface current density $\tilde{J}(\vec{r}', \omega)$ at a particular point $\vec{r}'$ is determined by the reflection characteristics (including amplitude of phase) of the meta-atom located at this very point, which thus sensitively depends on the punping conditions. Detailed parameters used in our calculation is presented in the following Table.

Table S3. Detailed parameters used in calculation

Meta-atom	$\tilde{J}_x(\vec{r}', \omega)$	W/O pump	$\lambda_{\text{pump}} = 515$ nm	$\lambda_{\text{pump}} = 1030$ nm
A	Amplitude	0.91	0.75	0.40
A	Phase ($\circ$)	0	-9.91	-132.6
B	Amplitude	0.86	0.67	0.37
B	Phase ($\circ$)	0	-118	-133.6

In our numerical calculations, the metasurface is not excited uniformly as it works like a square array antenna and results a diffraction pattern in far field. So, we add a 2D aperture function (Gaussian function $e^{-[\frac{r^2}{(\eta d)^2}]}$ with d being the side length of metasurface and η being a dimensionless parameter) in the dyadic green's function calculation to suppress the diffractions. In order to verify the necessity to use a 2D aperture function, we performed numerical calculations to study the radiation patterns of an array of electric dipoles with different aperture functions imposed (see Fig. S17). Here, the system we studied consists of electric dipoles arranged in a 66×66 lattice with a periodicity $\lambda/4$, and all excited dipoles have the same radiation amplitudes and phases. We find that the diffractions are indeed suppressed as we decrease of aperture parameter η.
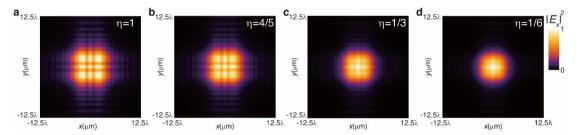
Fig. S17 Far field pattern of dipole array with different aperture functions.

a. $\eta = 1$ **b.** $\eta = 4/5$ **c.** $\eta = 1/3$ **d.** $\eta = 1/6$